# Transient Mold Fluid Flow with Well- and Mountain-Bottom Nozzles in Continuous Casting of Steel

R. CHAUDHARY, GO-GI LEE, B.G. THOMAS, and SEON-HYO KIM

Nozzle shape plays a key role in determining the flow pattern in the mold of the continuous-casting process under both steady-state and transient conditions. This work applies computational models and experiments with a one-third scale water model to characterize flow in the nozzle and mold to evaluate well-bottom and mountain-bottom nozzle performance. Velocities predicted with the three-dimensional $k$-$\varepsilon$ turbulence model agree with both particle- image velocimetry and impeller measurements in the water model. The steady-state jet velocity and angle leaving the ports is similar for the two nozzle-bottom designs. However, the results show that nozzles with a mountain-shaped bottom are more susceptible to problems from asymmetric flow, low-frequency surface-flow variations, and excessive surface velocities. The same benefits of the well-bottom nozzle are predicted for flow in the steel caster.

DOI: 10.1007/s11663-008-9192-0


## I. INTRODUCTION

BOTH the steady-state flow pattern and transient variations in the mold cavity are important to steel quality in continuous casting. Excessive meniscus velocities and surface turbulence lead to inclusion defects due to slag entrainment and level fluctuations in the mold.[1,2] Insufficient surface flows lead to meniscus freezing and other surface defects.[1,2] The mold flow pattern should be optimized to achieve a flat surface profile with stable meniscus velocities of the desired magnitude and minimum turbulence.

These important flow parameters are governed by the flow-control system (stopper rod or slide gate), nozzle geometry, Submerged Entry Nozzle (SEN) depth, casting speed, strand cross-sectional dimensions, argon-gas injection rate, slag behavior, and the application of electromagnetics.[1] The most influential and easily changed of these parameters are the nozzle port geometry details (port angle and port area) and the nozzle-bottom shape. In particular, the shape of nozzle bottom has an important influence on flow quality in the mold, including the surface velocity, surface-level profile, and turbulent variations that vary the frequency and magnitude of their fluctuations and asymmetries. This article applies a computational model and water-model experiments to analyze and compare the effect of two popular nozzle-bottom shapes on these flows.

R. CHAUDHARY, Graduate Student, is with the Department of Mechanical Science and Engineering, University of Illinois at Urbana–Champaign, Urbana, IL 61801. GO-GI LEE, Graduate Student, is with the Department of Materials Science and Engineering, Pohang University of Science and Technology, Pohang, Kyungbuk, 790-784, South Korea. B.G. THOMAS, Wilkins Professor of Mechanical Engineering, is with the Department of Mechanical Science and Engineering, University of Illinois at Urbana–Champaign. Contact e-mail: bgthomas@illinois.edu SEON-HYO KIM, Professor, is with the Department of Materials Science and Engineering, Pohang University of Science and Technology, Pohang, Kyungbuk, 790-784, South Korea.

Manuscript submitted July 17, 2008.

## II. PREVIOUS WORK

Owing to the difficulty of plant experiments and the similar kinematic viscosity of water and steel, much previous insight into mold fluid flow has been gained using water models.[1–6] Although most studies have focused on steady-state flow patterns, a few studies have noted transient phenomena.[3–11] Honeyands and Herberton[8] observed surface-level fluctuations in a thin-slab water model with a characteristic frequency that increased with casting speed, according to the time period for flow to circulate around the mold cavity. Gupta and Lahiri[5] observed flow asymmetries in the lower recirculation zones that alternated between sides like large-scale vortex shedding. Lawson and Davidson[9] used Laser Doppler Velocimetry (LDV) to measure oscillatory flow in a 0.33-scale thin-slab water model. Low-frequency oscillation modes had the most oscillatory energy, especially below 5 Hz in the jets, and below 0.2 Hz in the mold, overall. This is consistent with findings of Sivaramakrishnan *et al.*[11] and Assar *et al.*[3] from velocities measured in a 0.4-scale water model using Particle Image Velocimetry (PIV).

Many previous computational models have been applied to predict fluid flow exiting the nozzle.[12–15] Many researchers have shown that computational predictions of steady $k$-$\varepsilon$-based Reynolds-averaged Navier–Stokes (RANS) models[12–14,16–18] can reasonably predict the steady flow pattern measured in water models. Such models have been applied to investigate the effect of port angle and port shape on flow pattern and jet characteristics exiting the nozzle port.[12,15] Bai *et al.*[13,14] extended such a model to include multiphase effects and asymmetries from the slide-gate orientation[12] to investigate the effect of gas injection, casting

speed, gate opening, bubble size, port angle, and port shape.[13] Nozzle bottom was not found to have much effect on the steady-flow pattern. However, optimizing the steady-flow pattern is not as important as avoiding defects due to turbulent flow effects, such as transient level fluctuations.

Several recent models have been developed to study transient flow phenomena in the mold. Huang and Thomas[17] showed that an unsteady RANS model could simulate flow evolution in a caster and steel-slag interface level fluctuations induced by sudden changes of nozzle-inlet conditions. Others have applied Large Eddy Simulation (LES)[11,18–21] and showed it to match the time-average flow pattern measured in both water models[11,18–21] and in the steel caster with electromagnetic sensors.[21] Complex time-varying flow structures have been observed in the LES results,[19,20] even during nominally steady casting conditions. The velocity variations due to turbulence were compared with measurement. In spite of its known importance, few parametric studies have considered transient-flow variations. The effect of nozzle-bottom shape remains unclear and so is the subject of this work.

## III. WATER-MODEL EXPERIMENTS

A one-third scale water model was constructed to measure jet and surface velocities using both PIV and impeller-velocity meters. Vertical movement of a centered (aligned) stopper rod controls the flow rate through an annular space of approximately 2-mm minimum thickness. Water flows down the nozzle and into the mold through bifurcated ports angled 25 deg downward. Figure 1 shows the geometry in the front view (right) and side view (left). Water exits the bottom of the water-model mold through 11 outlets each with a 25 mm diameter. From there, water passes through a flow meter to the water-storage bath. Water is then

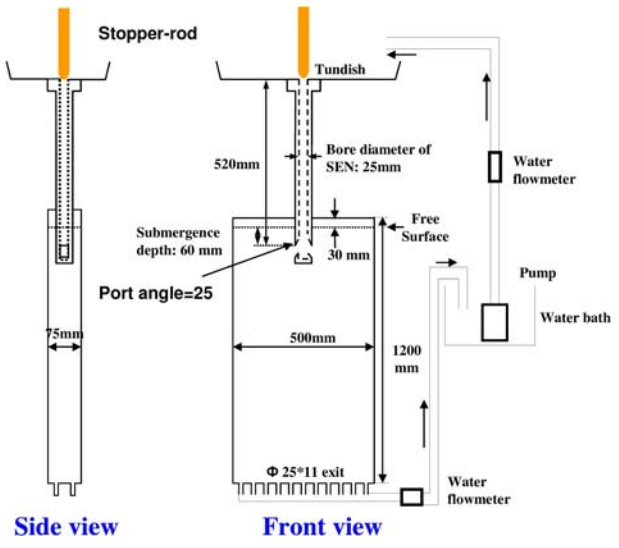


Fig. 1—Dimensions of one-third scale water model with well-bottom nozzle.

pumped back up to the tundish through a second flow meter, which is used by the stopper rod control system to maintain a constant flow rate. Table I provides details of the dimensions and casting conditions of the water model and the corresponding full-scale steel caster.

Figure 2(a) shows the nozzle geometry with the well-shaped bottom. Typically, the ports are oversized with a total port to bore ratio of 2.8. Figures 2(b) and (c) show close-up images of the well-bottom and mountain-bottom shapes. Both nozzles otherwise have the same geometry.

Velocity was measured using PIV just below the ports at the center-line plane of the mold for the well-bottom nozzle. A 2-mm-thick plane was illuminated using laser light, and velocity vectors were computed by digital analysis of snapshots taken 0.6 milliseconds apart. These velocities were measured every 0.14 seconds at each of the 125 × 56 grid points in the 285 mm wide and 130 mm high measurement window and time averaged over 360 seconds.

Velocities were also measured using impeller-velocity probes. Time-varying data was collected at a frequency of 1 Hz. Figure 3 shows the location and orientation of each sensor probe. Each probe is a 35 mm long open-ended tube (22 mm inner and 28 mm outer diameter) containing a small propeller that rotates in proportion with water speed. Jet velocities were measured by touching the probe to the port bottom and aligning it with the port angle (25 deg down). Surface velocity was

**Table I. Process Parameters for Experiments and Computations**

| Parameters | Water Model (One-Third Scale) | Steel Caster (Full Scale) |
|---|---|---|
| Stopper opening fraction | 0.11 | — |
| Nozzle port angle | 25 deg down | 25 deg down |
| Nozzle port area | 23.3 mm (width) × 26.7 mm (height) | 69.9 mm (width) × 80.1 mm (height) |
| Nozzle bore diameter | 25 mm | 75 mm |
| Nozzle outer diameter | 43 mm | 129 mm |
| SEN depth | 60 mm | 180 mm |
| Average port velocity | 0.512 m/s | 0.886 m/s |
| Fluid flow rate | 38.2 LPM | 595.4 LPM |
| Casting speed | 1.02 m/min | 1.76 m/min |
| Mold width | 500 mm | 1500 mm |
| Mold thickness | 75 mm | 225 mm |
| Domain width | 250 mm | 750 mm |
| Domain thickness | 37.5 mm | 112.5 mm (at the top) |
| Domain length | 1200 mm | 3600 mm |
| Shell | no | yes (Fig. 19) |
| Gas injection | no | no |
| $\rho_{fluid}$ | 998.2 kg/m$^3$ (water) | 7020 kg/m$^3$ (steel) |
| $\mu_{fluid}$ | 0.001003 kg/m s (water) | 0.006 kg/m s (steel) |
| $\rho_{slag}$ | — | 3000 kg/m$^3$ |

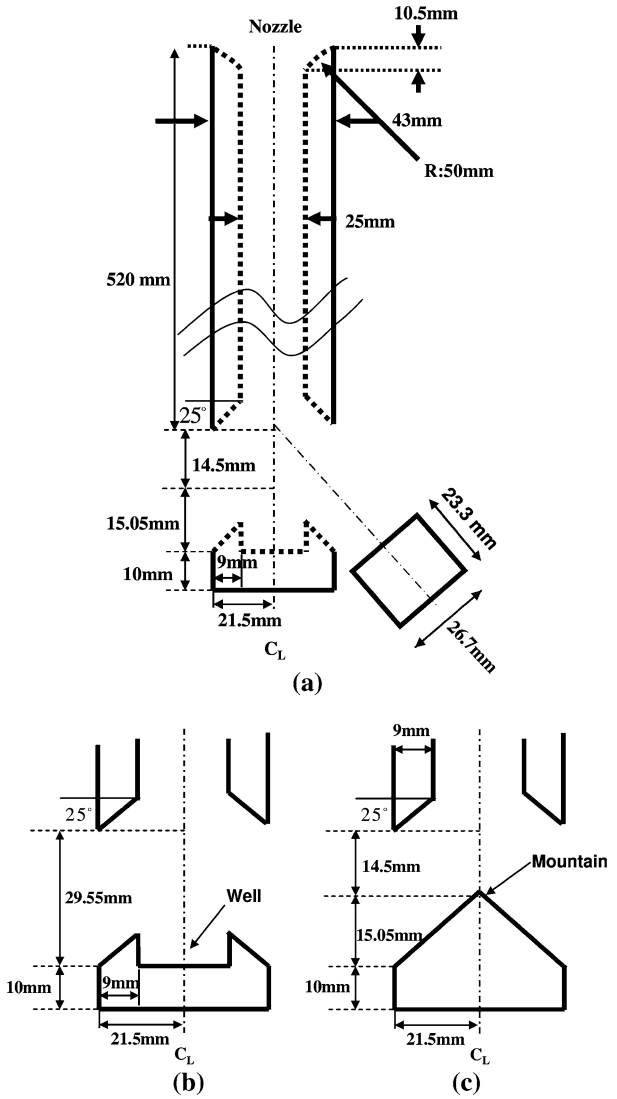


Fig. 2—Geometry of (*a*) nozzle and close-up of (*b*) well-bottom and (*c*) mountain-bottom shapes.

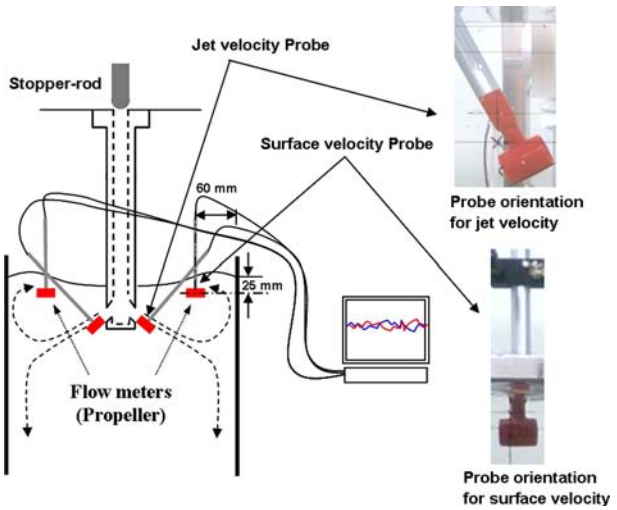


Fig. 3—Schematic of the impeller-velocity probe locations and orientations.

recorded 60 mm from each narrow face and 25 mm below the top free surface in the mold for both nozzles. The impeller-velocity probes have a total response time of approximately 10 seconds (*i.e.*, 0.1 Hz), including electrical response time (approximately 0.4 seconds to reach 63 pct of end value) and mechanical response time (for the vanes to respond to increase or decrease in flow). The probes are accurate over the velocity range of 0.02 to 5 m/s. For each case, mean velocities were averaged over 2000 seconds (except 1000 seconds for mountain surface) and corresponding isotropic turbulent kinetic energies were derived using standard root-mean-square,[22] assuming unmeasured components had the same variations. Finally, power spectra were calculated using the Mean Squared Amplitude (MSA) formulation.[19]

## IV. COMPUTATIONAL MODEL

A computational model has been formulated to simulate time-averaged turbulent-fluid flow in the nozzles and molds of well- and mountain-bottom nozzles. The steady-state, three-dimensional, incompressible, Navier–Stokes equations for momentum conservation are solved with the continuity equation, and the standard $k$ and $\varepsilon$ equations to model turbulence (Launder and Spalding[23]) are given by Thomas.[24] This approach needs a less-refined mesh and so is faster than the Direct Numerical Simulation (DNS) and LES methods, which are more accurate for transient flow.

The model domain contains only the liquid pool, so naturally it has straight walls for the water model. When modeling the steel caster, the domain has curved walls to match the shape of the solidification front, which was calculated using CON1D.[25] In addition to standard no-slip wall laws used on all solid boundaries,[22] downward velocity at the solidification front was fixed at the casting speed. To account for shell solidification, a source term of mass-sink per unit volume is added to the continuity equation as follows:[26,27]

$$\rho(\nabla \cdot \mathbf{v}) = S_{\text{mass}} = -\frac{\rho V_{\text{casting}} A}{V} \qquad [1]$$

where $\rho$ is the density of the fluid (kg/m$^3$); $V_{\text{casting}}$ is the casting speed; $A$ is the projection area in casting direction; and $V$ is the volume of the sink cells, which are 1-mm thick and extend over the domain-wall boundaries that represent the solidification front. A corresponding sink term for the momentum extracted per unit volume into the shell is added to each of the three ($x$, $y$, and $z$) momentum equations as follows:

$$\mathbf{S}_{\text{mom}} = -\frac{\rho V_{\text{casting}} A}{V} \mathbf{v} \qquad [2]$$

These terms were implemented with a User-Defined Function (UDF) C-language subroutine in FLUENT (ANSYS Inc., Lebanon, NH).[28] More details on these sinks terms are given by Creech and Rietow.[26,27]

Assuming symmetrical flow, twofold symmetry of the geometry enables a model of only a quarter of the nozzle

and strand to minimize computation. The nozzle and strand are discretized using approximately 19,000 and 0.136 million hexahedral cells, respectively, (Figure 4). To better model the flow entering the stopper region, a cylindrical portion of the tundish bottom (with 200-mm diameter and 150-mm height) is created around the top of the SEN. Figure 5 gives close-up views and meshes of the stopper and bottom regions of both nozzles. Average velocity with small values of $k$ and $\varepsilon$ ($10^{-5}$ $m^2/s^2$ and $10^{-5}$ $m^2/s^3$, respectively) were fixed at the circumference and top annular regions of the cylinder to match the flow rate for typical casting speed and dimensions (Table I).

To improve efficiency, nozzle flow is simulated first, using pressure-outlet boundary conditions. The velocities, turbulent kinetic energy, and dissipation rate at the outlet plane from the nozzle ports are then used as boundary conditions for the inlet surface to the strand. Hershey *et al.*[14] showed that this approach matches well with results of simulations that combine the nozzle and strand together. Convergence is easier because residuals in the important low-velocity regions of the strand are not overly influenced by small errors in the high velocities inside the nozzle. The meshes of the nozzle outlet and the strand inlet were identical with one to one mapping in order to ensure accurate flux balance between the two computational domains.

Free-slip boundaries with zero normal velocity were employed at the top free surface, and level fluctuations were calculated using pressure distribution along the free surface based upon potential-energy conservation.[17,29] Pressure-outlet boundary conditions were also used at strand exit. In case of reverse flow entering the lower recirculation zone, small values of $k$ and $\varepsilon$ ($10^{-5}$ $m^2/s^2$ and $10^{-5}$ $m^2/s^3$, respectively) were set at the strand-domain exit, along with 0 Pa gauge pressure.

The equations for the three momentum components, $k$, $\varepsilon$ and Poisson's equation for pressure correction are discretized using the Finite Volume Method (FVM) in FLUENT[28] with the first-order up-winding scheme for convection terms. These discretized equations are then solved for velocity and pressure using the Semi-Implicit Method for Pressure-Linked Equations (SIMPLE), starting with initial conditions of zero velocity.[29] Standard wall laws were used as boundary conditions.[30] Finally, $k$ and $\varepsilon$ equations are solved. The turbulent-viscosity field is obtained from $k$ and $\varepsilon$ and added to the molecular viscosity to obtain effective viscosity for the next step update. The segregated solver in FLUENT was used to solve all equations. In all

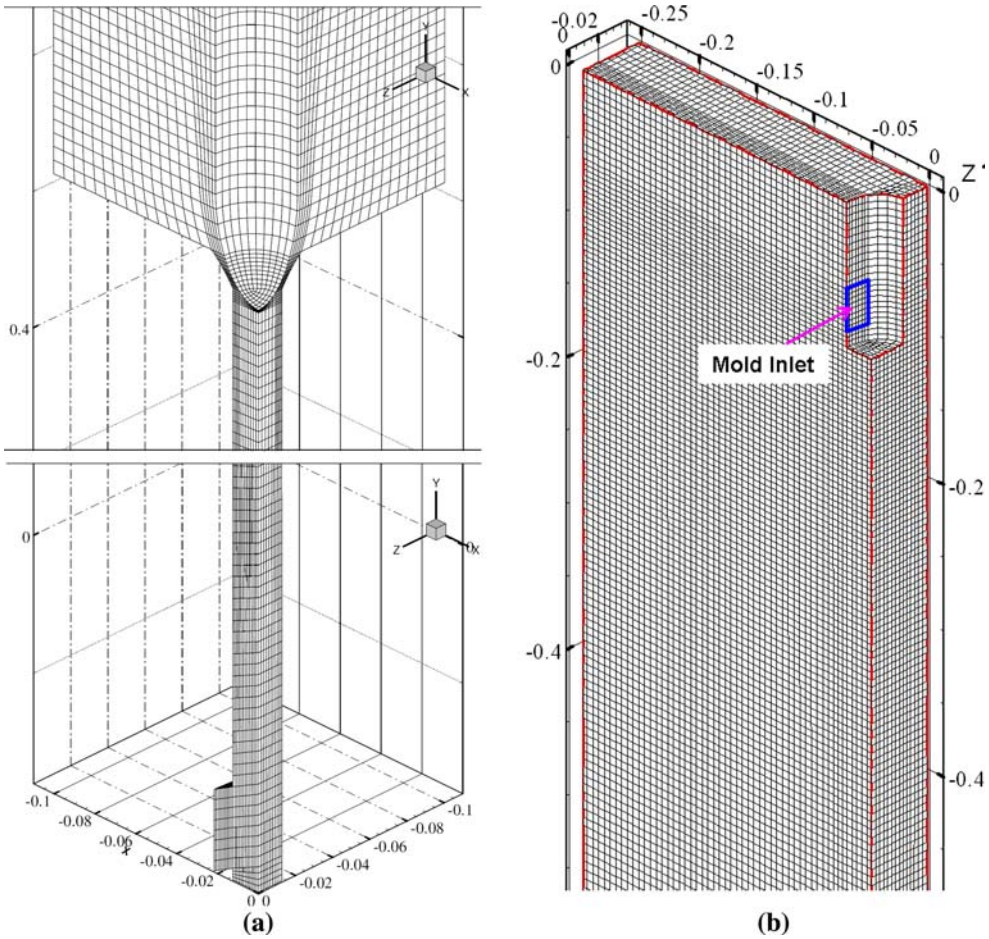


Fig. 4—Isometric view of (*a*) well-bottom nozzle and (*b*) strand quarter domains and meshes.

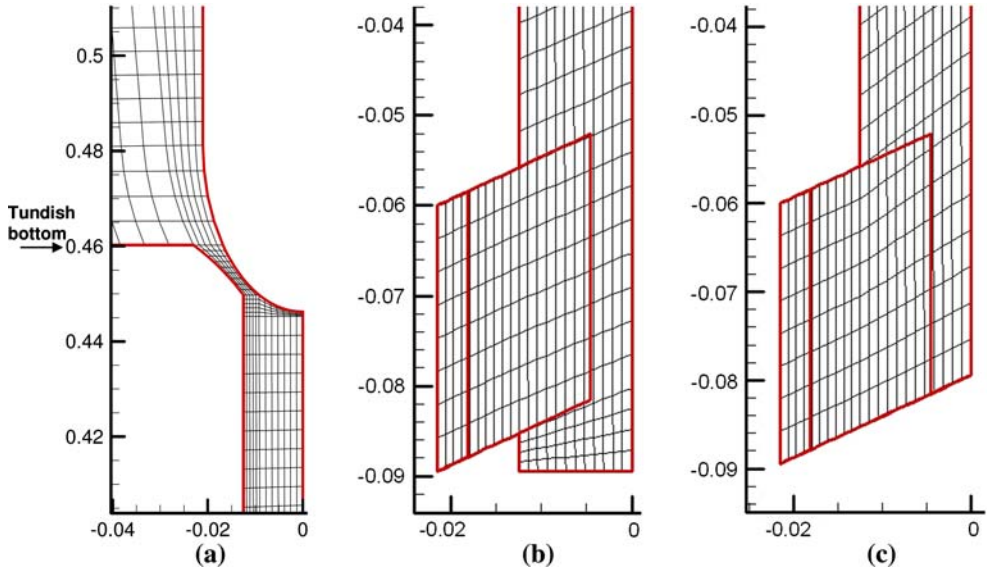


Fig. 5—Mesh closeup of (*a*) stopper-rod head region, (*b*) bottom region of well-bottom nozzle, and (*c*) bottom region of mountain-bottom nozzle.

simulations, convergence was defined when all scaled residuals were reduced below $10^{-4}$. All computations were performed on a computer with a 2.66 GHz Intel Xeon processor (Intel Corp., Santa Clara, US) and 4.0 GB RAM. Each nozzle simulation converged in approximately 15 minutes and required approximately 1000 iterations. Strand simulations took approximately 3 hours with 7600 iterations for the mountain-bottom nozzle and approximately 2 hours with 4000 iterations for the well-bottom nozzle.

## V. MODEL VALIDATION

The computational model predictions are validated here by comparing with the time-averaged PIV, impeller velocity, and turbulence measurements. Figure 6(a) shows the PIV- measurement window, which extends down from the port bottom, and Figure 6(b) shows the average velocity-magnitude contours. The bottom of the SEN extends into the top of the frame. The maximum velocity is 1.022 m/s on the upper-left side. On the upper-right side, shadow effects from the nozzle spoil the PIV measurements in the red-triangle region.

Figures 6(c) and (d) give velocity contours modeled using second-order and first-order upwind convection schemes, respectively. With second-order upwinding (Figure 6(c)), the maximum velocity is 1.09 m/s, and the jet is thinner, bending upward slightly. The jet shape matches most closely with the PIV measurements. With first-order upwinding (Figure 6(d)), numerical diffusion makes the jet thicker and more stable, and the maximum speed decreases to 1.02 m/s. These results match closer to the measured jet velocity and with the shape of the flow pattern deeper in the caster. Moreover, the second-order scheme is less stable and did not converge for the mountain-bottom nozzle. Thus, the first-order scheme was used in further simulations.

A comparison of impeller measurements of velocity and turbulence with computational- model predictions is summarized in Table II. The velocity predictions agree with the time average of the measurements about as well as the measurements on the right and left sides agree with each other. Moreover, the trends are consistent. The well-bottom nozzle velocity measurements show little variation between sides and agree with the predictions within 1 pct. The mountain-bottom nozzle exhibits significant asymmetry between left and right, indicating that the time-averaging period was too short for this nozzle. The predictions agree within these variations. For example, surface velocity averaged over the last 500 seconds is 0.180 m/s, which matches exactly with the prediction.

Agreement with the turbulent kinetic-energy measurements is not quite as good. The measured turbulence of the jet exiting the ports is one to two orders of magnitude smaller than at the surface. This is contrary to expectations that the jet should be more turbulent, as predicted with the computational model. This is believed to be due to the known inability of the impeller probe to respond to the high-frequency fluctuations that dominate the jet turbulence, due to the inertia of the impeller. In addition, the fixed orientation of the probe is unable to measure nonaxial fluctuations, which were observed to be significant in this region. Agreement is much better at the top surface, which has lower-frequency fluctuations. Measurements and predictions agree reasonably for the mountain-bottom nozzle and are in the same range for the well-bottom nozzle. Moreover, the trends agree. Thus, the model predictions and measurements are used together to understand flow in the remainder of this work.

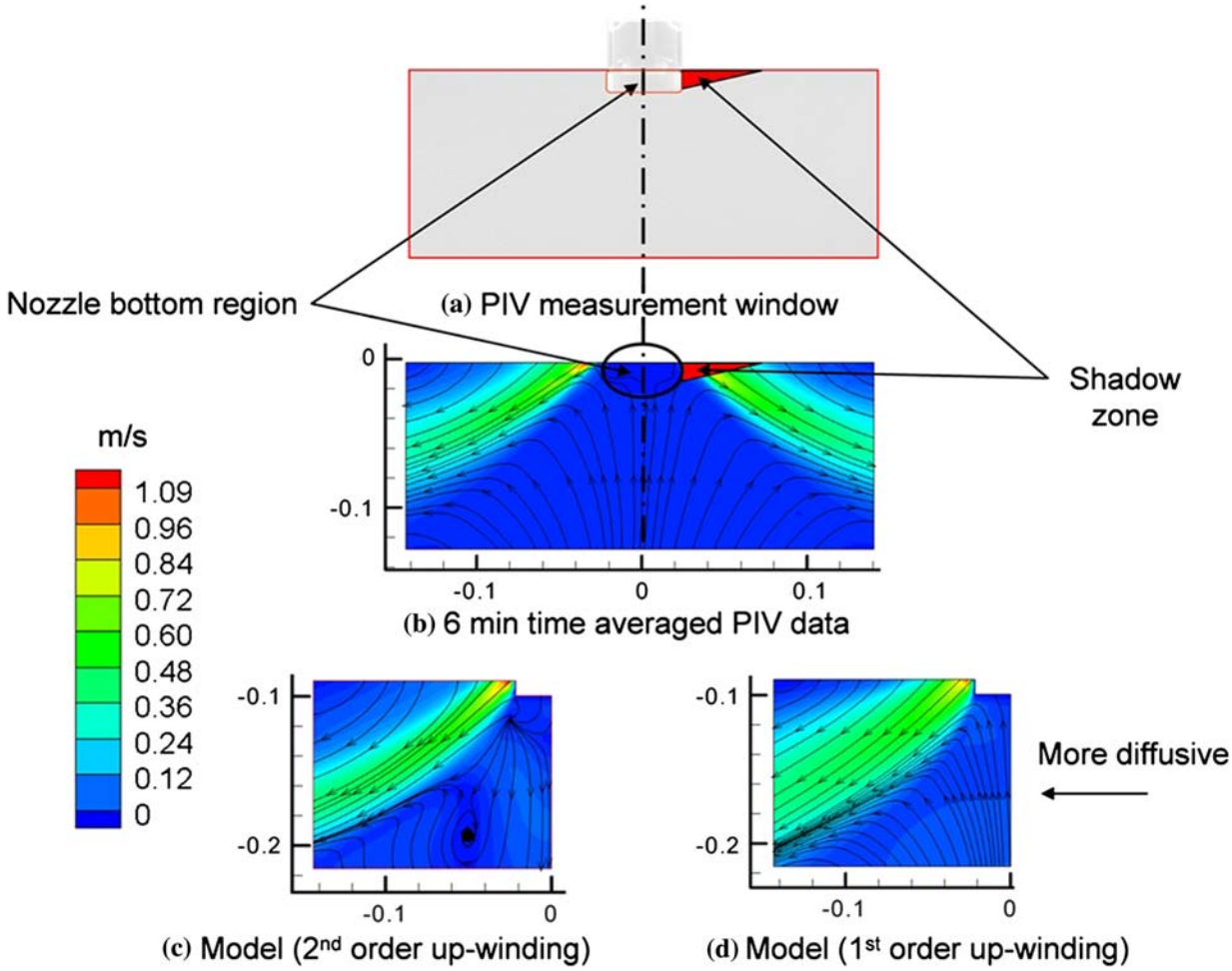


Fig. 6—(*a*) PIV measurement window in water model with well-bottom nozzle with (*b*) PIV measured velocity (time averaged over 6 min), (*c*) model velocity and streamlines (second-order up-winding), and (*d*) model velocity and streamlines (first-order up-winding).

**Table II. Comparison of Predictions and Impeller Measurements (a) in Jet and (b) near Top Surface**

| | | | | Turbulent Kinetic Energy ($m^2/s^2$) ($\times 10^{-3}$) | | |
|---|---|---|---|---|---|---|
| | Water Model | | | Water Model | | |
| | Left Side | Right Side | Fluent | Left Side | Right Side | Fluent |
| (a) Jet Velocity (m/s) | | | | | | |
| Well bottom | 0.687 | 0.685 | 0.69 | 0.0611 | 0.0898 | 22.3 |
| Mountain bottom | 0.957 | 0.944 | 0.92 | 0.0216 | 0.0087 | 20.1 |
| (b) Horizontal-Surface Velocity (m/s) | | | | | | |
| Well bottom | 0.103 | 0.115 | 0.11 | 0.31 | 0.38 | 1.4 |
| Mountain bottom | 0.148 | 0.166 | 0.18 | 2.23 | 3.14 | 2.4 |

## VI. COMPUTATIONAL RESULTS

### A. *Nozzle Flow*

Figure 7 gives the velocity contours and vectors near the stopper-rod head and bottom region of both nozzles. The maximum velocity is 3.8 m/s and is found in the thinnest part of the annular region between the stopper rod and the tundish bottom. Figure 8 compares streamlines, and Table III quantifies the jet characteristics[12] for both nozzles. The jet in the well-bottom nozzle is more diffusive and thicker with a smaller backflow zone (27 pct *vs* 30 pct in mountain bottom). In the mountain-bottom nozzle, flow goes straight along the side of the mountain with a high velocity, producing a thinner and less diffusive jet with smaller horizontal spread and vertical jet angles (Table IV).

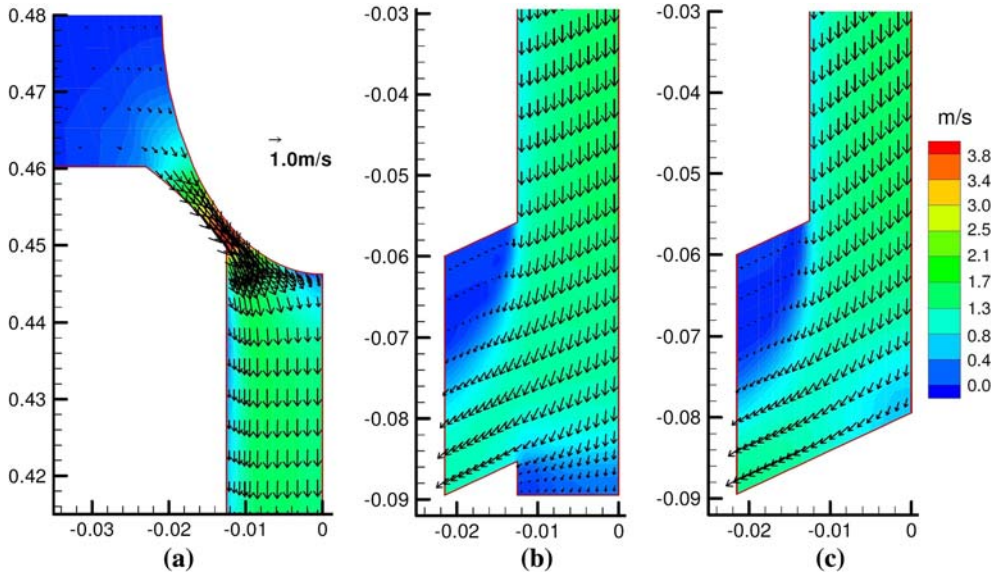


Fig. 7—Comparison of velocity in (*a*) stopper-rod head region, (*b*) bottom region of well-bottom nozzle, and (*c*) bottom region of mountain-bottom nozzle.

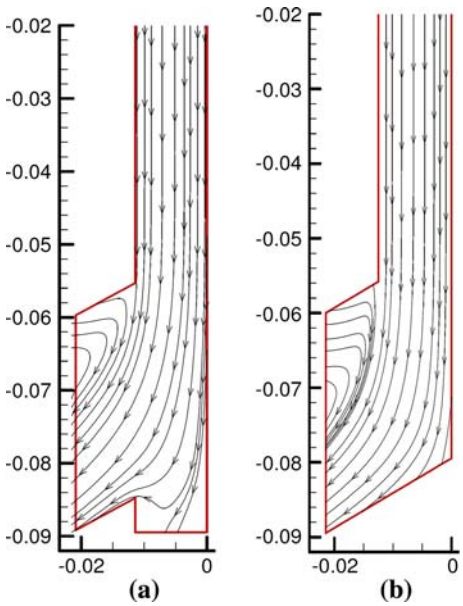


Fig. 8—Comparison of streamlines in (*a*) well- and (*b*) mountain-bottom nozzles of water model.

**Table III. Computed Jet Characteristics in Water Model**

| Weighted Average Parameter | Well-Bottom Nozzle | Mountain-Bottom Nozzle |
|---|---|---|
| Port *x* velocity (outward) (m/s) | 0.75 | 0.92 |
| Port *y* velocity (downward) (m/s) | 0.48 | 0.52 |
| Port *z* velocity (horizontal) (m/s) | 0.065 | 0.076 |
| Port turbulent kinetic energy ($m^2/s^2$) | 0.040 | 0.018 |
| Port turbulent dissipation rate ($m^2/s^3$) | 2.11 | 0.64 |
| Vertical jet downward angle (deg) | 32.8 | 29.3 |
| Horizontal jet angle (deg) | 0 | 0 |
| Horizontal spread (half) angle (deg) | 5.0 | 4.7 |
| Average jet speed (m/s) | 0.89 | 1.06 |
| Back-flow zone | 27 pct | 30 pct |

Figure 9 compares velocity contours and vectors at port exit. Secondary flows from the mountain-bottom nozzle are weaker as flow is directed more toward the narrow face. Figure 10 gives velocity contours and vectors on lines angled 25 deg from the port bottom in the mold region close to SEN. The maximum velocity is close to the port bottom in both ports with a steeper, thicker jet (Figure 7 and Table III) from the well-bottom nozzle. Higher outward, downward, and horizontal weighted-average jet velocities exiting the mountain-bottom nozzle are observed in both the experiments and computations. Turbulent kinetic energy is much higher in the well-bottom nozzle, with higher-frequency fluctuations causing a more dissipative jet.

## B. *Mold Flow Pattern*

Figure 11 presents the mold flow patterns at the midplane between wide faces for both nozzles. The higher dissipation rate leaving the port of the well-bottom nozzle causes the jet turbulent kinetic energy to decrease more as it moves through the mold. This thicker and more diffusive jet thus loses its momentum faster as it splits into upper and lower recirculation zones with weaker flow along the narrow face. Maximum velocity is found near the bottom of port exit and is 1.23 m/s with the well-bottom nozzle. With the mountain-bottom nozzle, the jet is faster (1.31 m/s), which leads to higher surface velocity. The latter jet also

Table IV. Evaluation of Well-Bottom and Mountain-Bottom Nozzle Flow Characteristics

| Nozzle Type | Jet Velocity | | Surface Velocity | | Asymmetry (Due to Flow Transients) |
|---|---|---|---|---|---|
| | Average Velocity | Fluctuations | Average Velocity | Fluctuations | |
| Well bottom | low (thick jet) | high (high frequency) | Low | low (high frequency) | low |
| Mountain bottom | high (thin jet) | low (low frequency) | High | high (low frequency) | high |

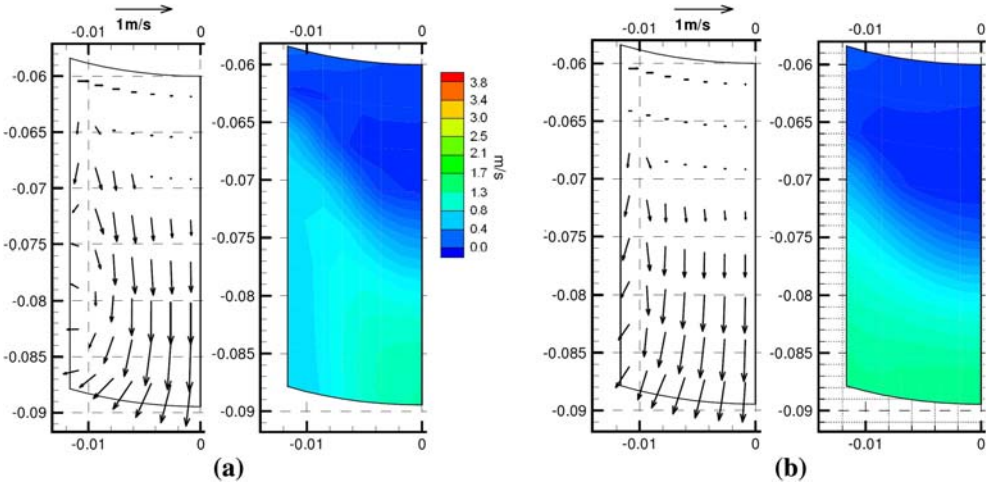


Fig. 9—Comparison of the port velocities in (*a*) well- and (*b*) mountain bottom nozzles.

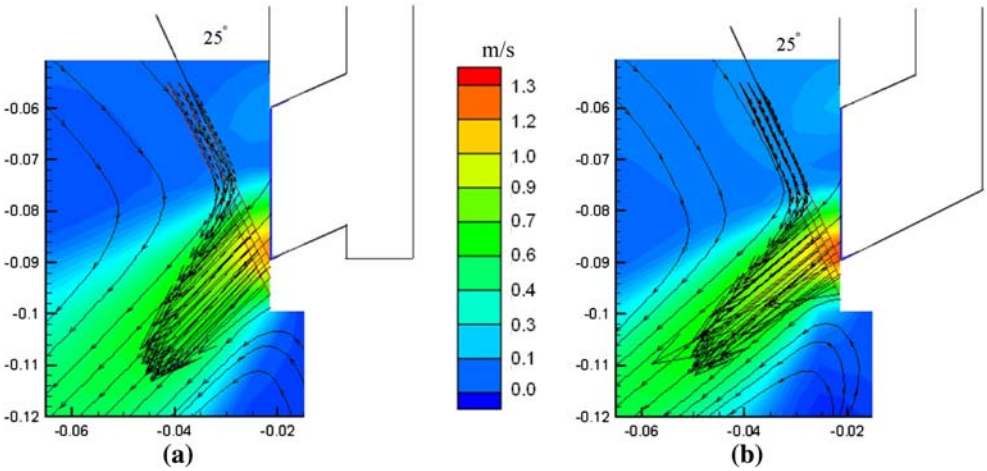


Fig. 10—Calculated jet-velocity vectors and speed contours near nozzle at mold center plane in (*a*) well- and (*b*) mountain-bottom nozzles.

bends upward more as it crosses the mold, further contributing toward the higher surface velocity. Also, the lower recirculation zone is predicted to break up into more complex flow structures.

Figure 12 gives the vertical speed along the midplane vertical line at 10 mm from the narrow face. The mountain-bottom nozzle has faster flow in the upper recirculation zone. The jet impinges the narrow face at 180 mm below the top free surface with both nozzles. The free surface level for both nozzles is given in Figure 13 at the midplane between the wide faces. The surface is raised near the narrow face and SEN, as common with a double-roll flow pattern. The mountain-bottom nozzle gives approximately 2.5 times higher surface waves, owing to its approximately 1.5 times higher horizontal surface velocity (Figure 14(a)). This higher surface velocity agrees with the measurements (Figure 16) and is due to the stronger flow up the narrow face.

The turbulent kinetic energies predicted for the two nozzles at the free surface are given in Figure 14(b). The mountain-bottom nozzle gives approximately 5 times higher turbulent kinetic energy compared to the well bottom. This is due to the low frequency and high-magnitude fluctuations in the surface velocity for this nozzle.

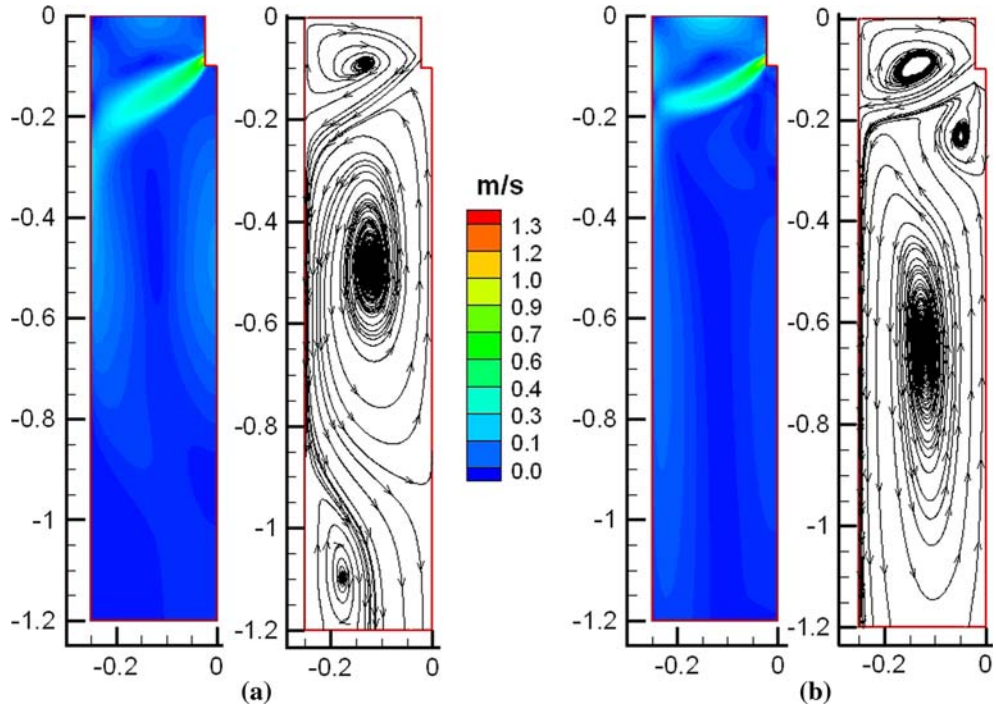


Fig. 11—Velocity contours and streamlines at the midplane between wide faces with (*a*) well- and (*b*) mountain-bottom nozzles in water-model mold.

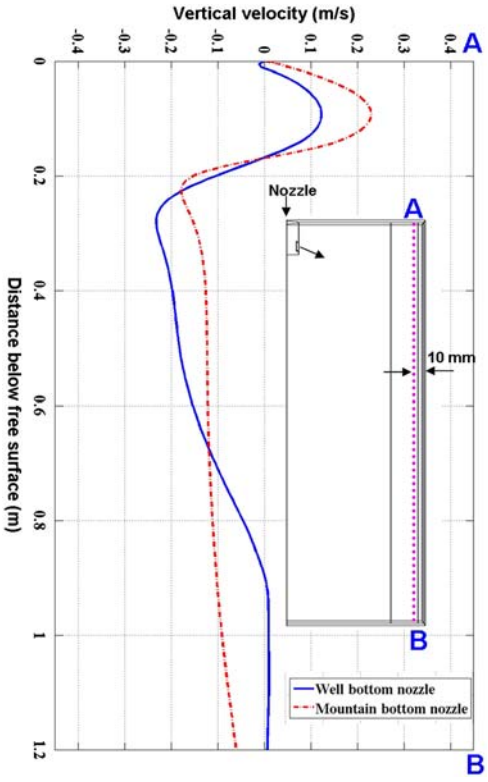


Fig. 12—Vertical velocity at 10 mm from narrow face at the midplane between wide faces with well- and mountain-bottom nozzles in the water-model mold.

## VII. WATER MODEL RESULTS

### A. *Jet Velocity*

Figure 15 shows the jet velocities measured on the left and right sides with the impeller probe. Time-averaged jet velocities with the well-bottom nozzle are approximately 0.686 m/s and are quite symmetric, with the left and right sides matching within approximately 0.3 pct over 2000 seconds. In the mountain-bottom nozzle, the corresponding jet velocities average 0.950 m/s, which is significantly higher. They are also less symmetric, with approximately 1.4 pct higher velocity on the left side, which indicates stronger, lower-frequency variations.

### B. *Surface Velocity*

Figure 16 shows the measured histories of the horizontal velocities near the surface on the left and right side of the mold for both nozzles, along with the their time-averaged values. For the well-bottom nozzle, time-averaged horizontal-surface velocities are approximately 0.109 m/s, with the right side 11.6 pct higher than the left. The mountain-bottom nozzle has more than 50 pct higher average surface velocities, 0.157 m/s, due to the higher jet velocity. Its asymmetry is also higher, with 12.1 pct higher velocity on the right side. Relative to the jet, these surface flow results show that asymmetry increases as the flow travels through the mold. Furthermore, the mountain-bottom nozzle is more susceptible to asymmetric flow.

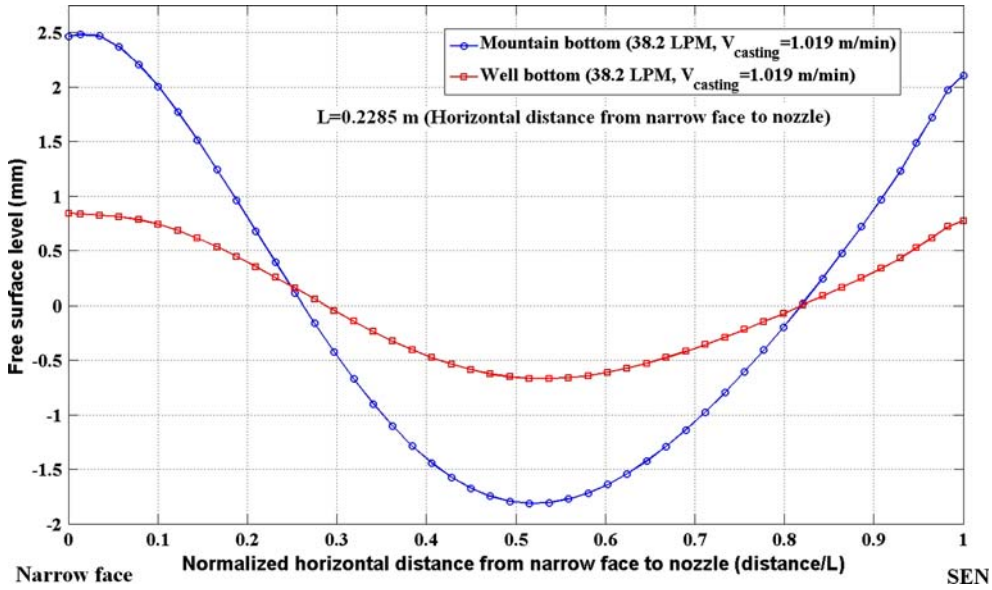


Fig. 13—Free surface-level comparison in well- and mountain-bottom nozzles of water-model mold.

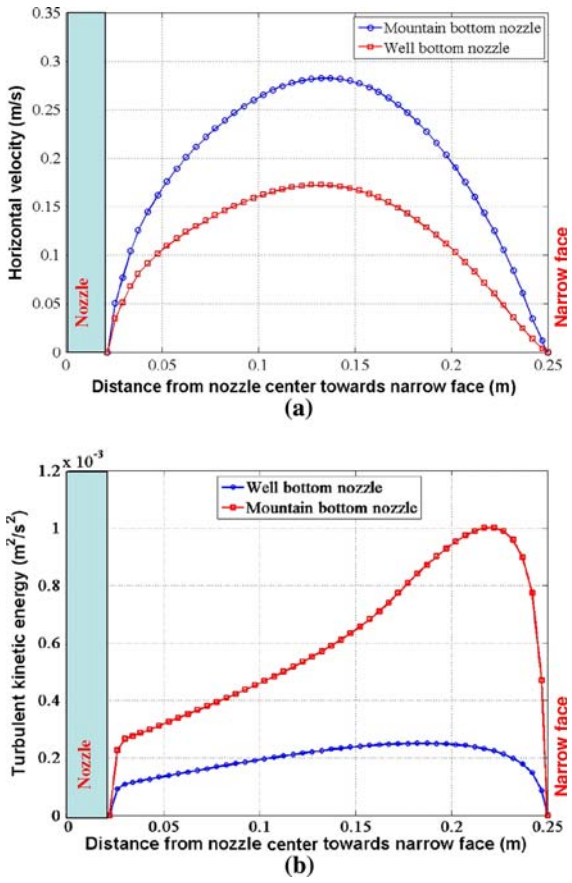


Fig. 14—Comparison of (*a*) horizontal speed and (*b*) turbulent kinetic energy along the centerline at the free surface in two nozzles of water-model mold.

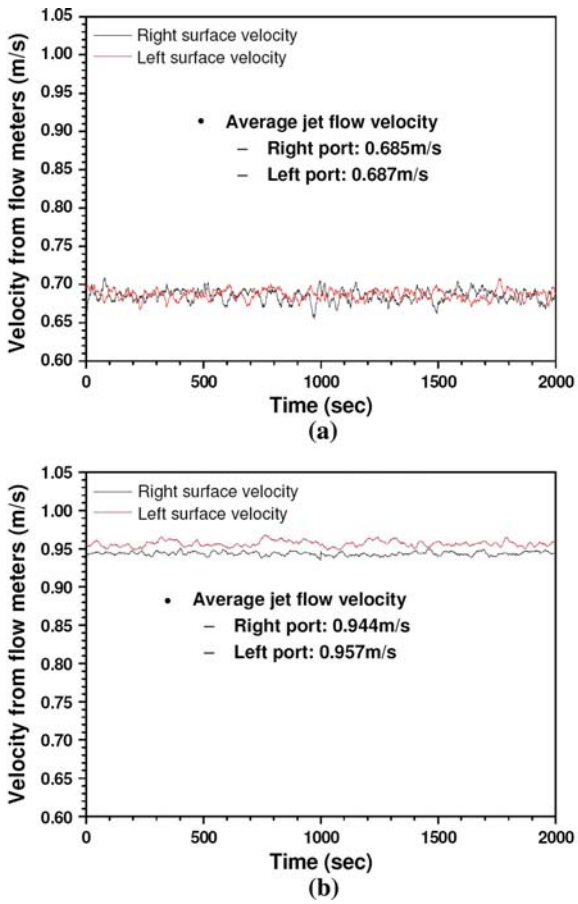


Fig. 15—Instantaneous jet speed measured in the water-model mold with (*a*) well- and (*b*) mountain-bottom nozzles.

## C. *Velocity Fluctuations*

Power spectrum of the jet and surface velocity fluctuations of both nozzles are shown in Figures 17 and 18, respectively. Due to an approximate 10 seconds response time of the impeller probe, only energies for frequencies up to 0.1 Hz are plotted. In all cases, most

of the energy is found in low frequencies. The general drop in energy observed with increasing frequency matches previous work.[10,15] An exception is the small peak found at approximately 0.07 Hz (approximately 14 seconds). The same frequencies dominate in the jet and surface for both nozzles. Energy in the jet is higher in the well-bottom nozzle, especially at frequencies above 0.01 Hz. This is due to strong recirculation observed in the bottom of the nozzle (Figure 8). The mountain nozzle deflects the jet smoothly toward the ports, slicing through the flow, similar to a knife-edge. This allows the jets to retain more of their momentum but with less turbulence. This causes the trend in energy spectrum at the surface to reverse. The mountain-bottom nozzle experiences much greater surface-velocity fluctuations. Figure 18 shows the increase to be more than an order of magnitude at frequencies ranging from 0.002 to 0.035 Hz, which corresponds with time periods of 33 to 500 seconds. This finding is also shown in Figure 16. The well- bottom nozzle has energy distributed over a wider frequency range in both jet and surface velocities.

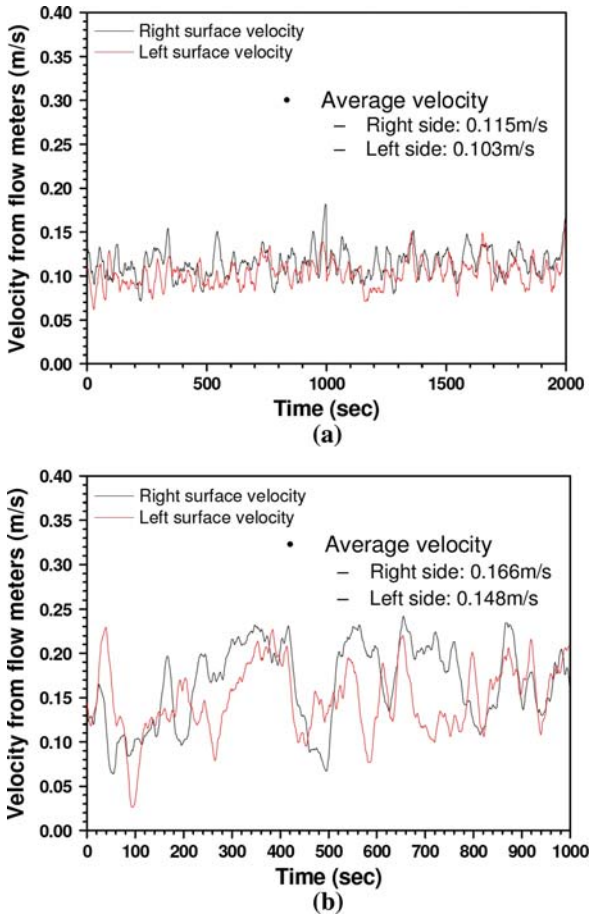


Fig. 16—Instantaneous surface speed measured in water-model mold with (*a*) well- and (*b*) mountain-bottom nozzles.

### D. *Mechanism*

The increased velocity fluctuations and left-right asymmetry of the mountain-bottom nozzle are explained with Figure 19. Transient variations in nozzle flow may send higher velocity down one side of the nozzle. The mountain bottom slices the flow, sending this higher-velocity flow directly out the adjacent port. The well bottom, on the other hand, mixes the flow so the jets exiting the ports are less sensitive to asymmetries.

## VIII. COMPARISON OF WATER MODEL WITH FULL-SCALE STEEL CASTER

Simulations of a full-scale steel caster with well-bottom nozzle were performed to evaluate the water-model findings. The laboratory water model has several differences from the real caster as follows: (1) geometric

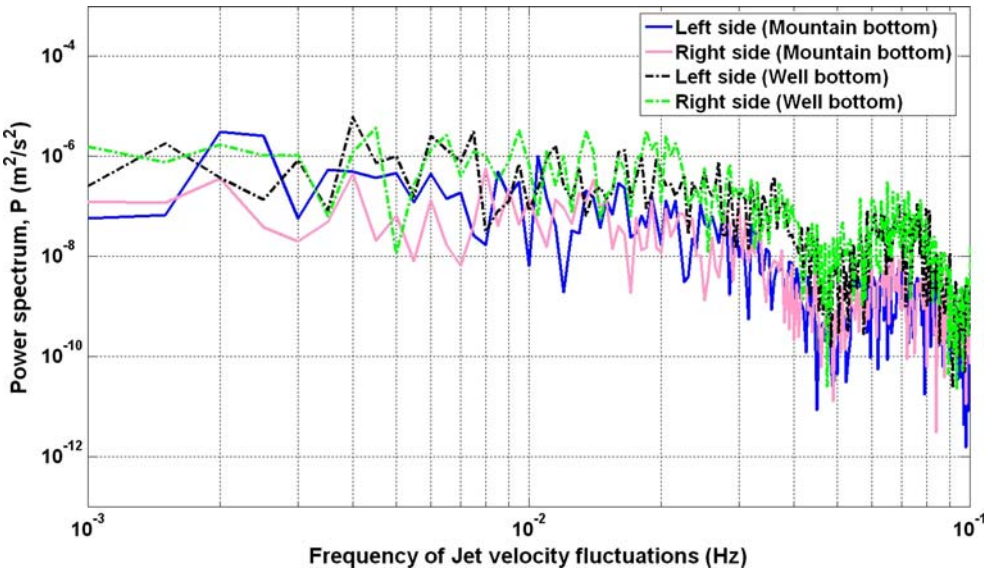


Fig. 17—Power spectrum of jet-velocity fluctuations measured in water model with well- and mountain-bottom nozzles.

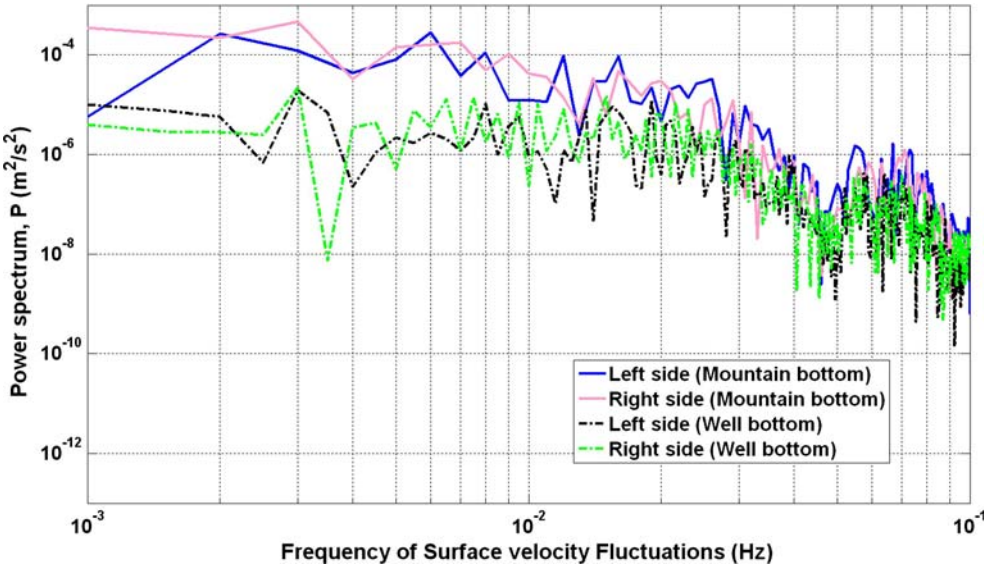


Fig. 18—Power spectrum of surface-velocity fluctuations measured in water model with well- and mountain-bottom nozzles.

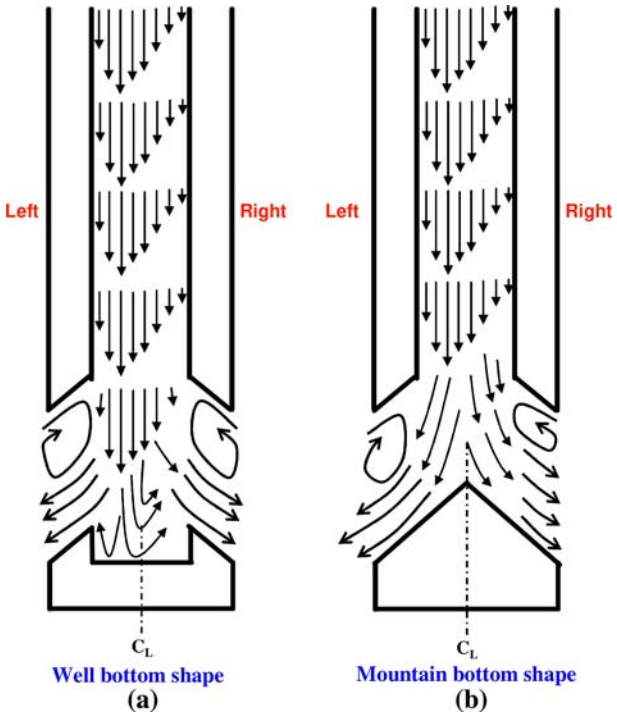


Fig. 19—Schematic of effect of flow asymmetry in (*a*) well- and (*b*) mountain-bottom nozzles.

scaling of all linear dimensions to one-third scale; (2) no solidifying shell and stationary walls; (3) a domain bottom with water exiting through circular holes in a horizontal plate instead of a very long, gradually tapering flow domain; and (4) air above the free surface instead of powder, sintered, and liquid-slag layers. A steel caster was simulated with and without the solidifying shell for conditions in Table I. Figure 20 gives the shell-thickness profiles down the wide and narrow faces calculated using CON1D.[25]

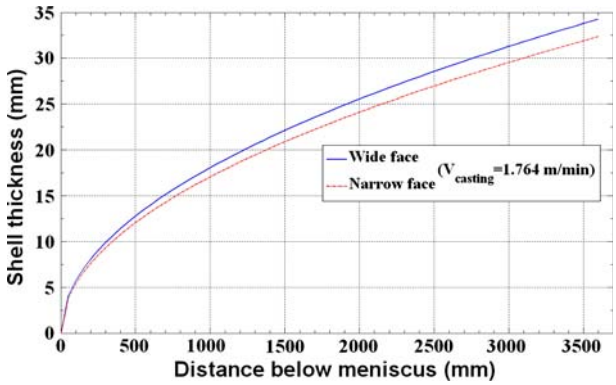


Fig. 20—Shell-thickness profile from CON1D.

Figure 21 presents the velocity contours and streamlines at the midplane between wide faces in the steel caster with the solidifying shell. The casting speed for the full-scale caster matches the Froude number of 0.005 of the water model. The flow pattern is generally similar to the water model. Comparison of horizontal-surface velocity between water model (after converting to full scale) and the steel caster is given in Figure 22. The horizontal axis is non-dimensionalized to compare both water model and caster. The vertical axis is simply the horizontal velocity for the steel caster. Horizontal velocity for the water model was multiplied by 1.732 (the square root of the length scale of 3), according to the Froude criterion. The horizontal velocity in the water model falls in between the caster velocities with and without the solidifying shell. Note that flow in the water model is in the transition regime (Re = 2200 based on strand-hydraulic diameter), while the steel caster is fully turbulent (Re = 13,500). The water-model velocities would match the caster without the shell if it was fully turbulent.

The maximum surface velocity predicted in the real full-scale steel caster with the well-bottom nozzle is approximately 0.3 m/s, which is in the safe operating window of 0.2 to 0.4 m/s.[2] Maximum surface velocity with the mountain-bottom nozzle is predicted to be approximately 0.5 m/s, which is above the upper limit suggested by Kubota[2] to avoid flow problems, such as slag entrainment. Thus, the well-bottom nozzle is preferred over the mountain-bottom nozzle for this steel caster and conditions. If casting conditions produced very small surface velocities, then the mountain-bottom nozzle might appear to be better. However, the results of this work suggest that changing the flow pattern in some other way and using the well-bottom nozzle is the best solution.

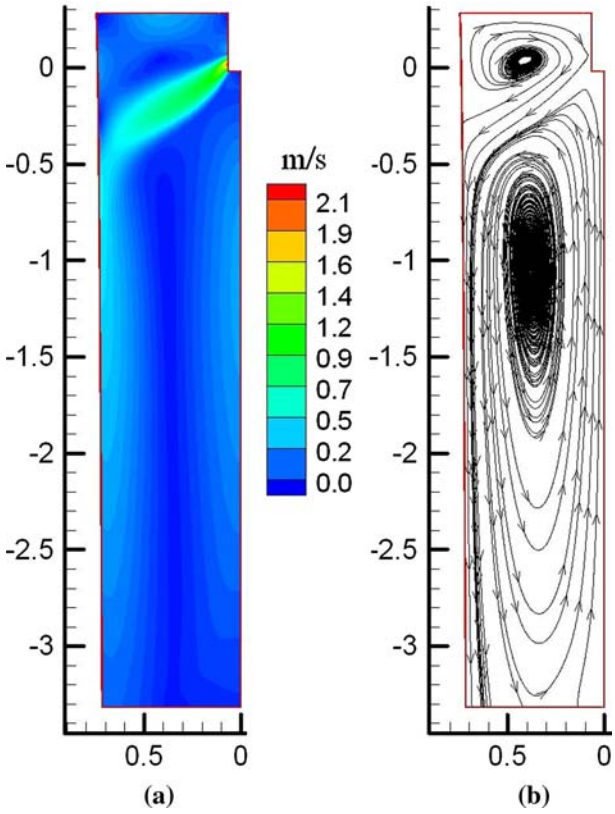


Fig. 21—Velocity at midplane between wide faces: (*a*) contours and (*b*) streamlines in full-scale steel caster with solidifying shell in the mold of well-bottom nozzle.

The free surface-level profile comparison between water model and steel caster is given in Figure 23. The free surface level without shell and air above matches most closely with the water model, as expected, although the water model underpredicts by a factor of 2.3. Introducing the shell and adding slag both increase the profile variations. Thus, the water model underpredicts surface-level variations in the caster using Froude scaling.

## IX. SUMMARY

This work investigates well-bottom and mountain-bottom type nozzles both experimentally and numerically. The computational model agrees very well with measured velocities in all cases but over predicts turbulent kinetic energy in the jet and surface of the well-bottom nozzle perhaps due to time resolution (approximately 0.1 Hz) of the impeller probe and fluctuations being higher frequency. The measured surface turbulence in mountain-bottom nozzle matches well with the simulations. Based upon experiments and the validated computational model, the following

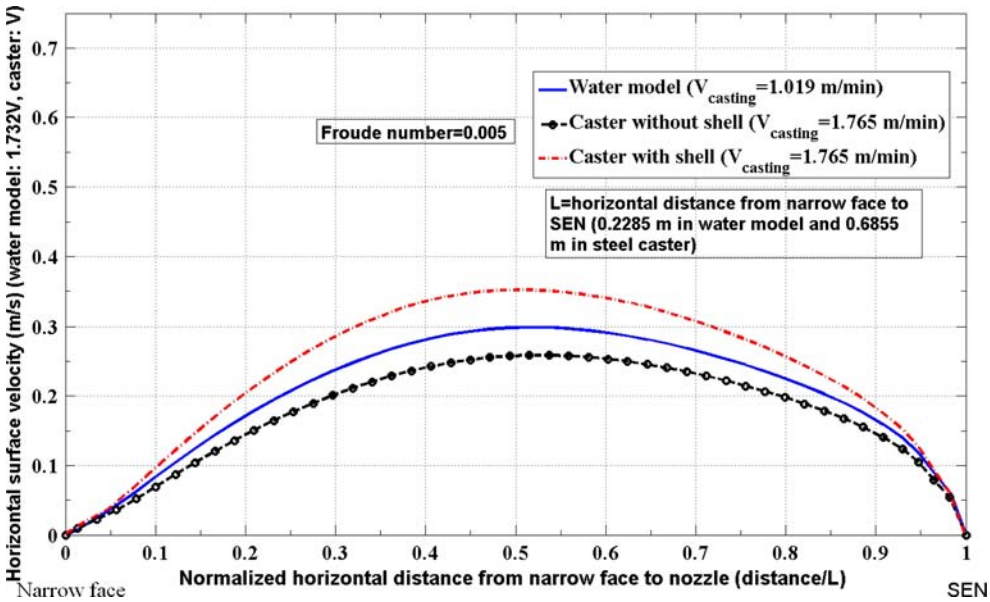


Fig. 22—Comparison of surface velocities in mold of one-third scale water model and steel caster using Froude-number similarity (well-bottom nozzle).

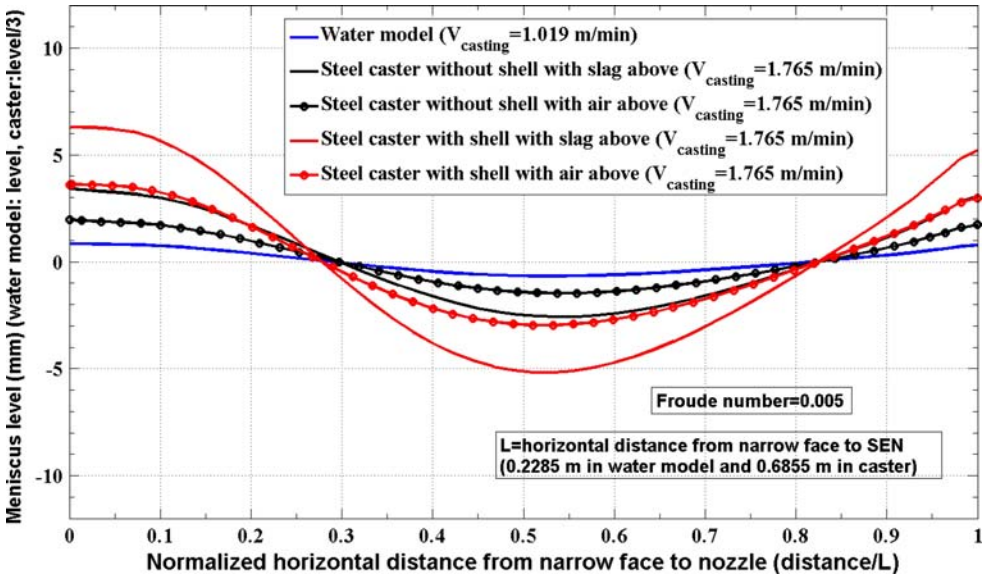


Fig. 23—Comparison of liquid level in one-third scale water model and steel caster with solidifying shell using Froude-number similarity (well-bottom nozzle).

conclusions have been drawn and are also summarized in Table IV.

1. The jet from the well-bottom nozzle is thicker, steeper-downward, and more diffusive, with higher turbulent kinetic energy and dissipation rate, relative to the mountain-bottom nozzle jet.
2. The mountain-bottom nozzle produces a thinner jet with stronger, lower-frequency fluctuations, making it more asymmetrical in short-term time averages.
3. Velocity fluctuations decrease in frequency from the jet leaving the ports to the surface in both nozzles.
4. The mountain-bottom nozzle produces approximately 50 pct higher surface velocity in the mold.
5. The mountain-bottom nozzle causes surface-velocity fluctuations with almost 96 pct of total measured energy at lower frequencies (33- to 500-second time periods).
6. The higher velocity and turbulence at the surface causes higher variation in surface-level profile, more level fluctuations, and easier slag entrainment with the mountain-bottom nozzle.
7. Full-scale steel casters have a proportionally higher speed, including higher surface velocities and level fluctuations, which are reasonably characterized by Froude similarity. The preceding water-model findings are predicted to hold in the steel caster as well.
8. With less surface fluctuations, the well-bottom nozzle is recommended over the mountain-bottom shape for steel quality.

## ACKNOWLEDGMENTS

The authors thank Young-Jin Jeon and Professor Hyung-Jin Sung, Department of Mechanical Engineering, KAIST (South Korea), and Seong-Mook Cho, POSTECH (South Korea), for help with the PIV measurements. They also thank POSCO, Oh-Duck Kwon, Shin-Eon Kang, and POSCO Technical Research Laboratories for relevant data and providing the water model and ANSYS Inc. for supplying FLUENT. Support from the Continuous Casting Consortium, University of Illinois at Urbana–Champaign, POSCO, South Korea (Grant No. 4.0002397.01) and the National Science Foundation (Grant No. DMI 05-00453) is gratefully acknowledged.

## REFERENCES

1. B.G. Thomas: in *Making, Shaping and Treating of Steel*, 11th ed., vol. 5, Casting volume, A. Cramb, ed., AISE Steel Foundation, Pittsburgh, PA, 2003, pp. 14.1–14.41.
2. J. Kubota, K. Okimoto, A. Shirayama, and H. Murakami: *Steelmaking Conf. Proc.*, Iron and Steel Society, Warrendale, PA, 1991, vol. 74, pp. 233–41.
3. M.B. Assar, P.H. Dauby, and G.D. Lawson: *Steelmaking Conf. Proc.*, ISS, Warrendale, PA, 2000, pp. 397–411.
4. D. Gupta and A.K. Lahiri: *Metall. Mater. Trans. B*, 1996, vol. 27B, pp. 757–64.
5. D. Gupta and A.K. Lahiri: *Steel Res.*, 1992, vol. 63 (5), pp. 201–04.
6. B.G. Thomas, X. Huang, and R.C. Sussman: *Metall. Mater. Trans. B*, 1994, vol. 25B, pp. 527–47.
7. B.G. Thomas and L. Zhang: *ISIJ Int.*, 2001, vol. 41 (10), pp. 1181–93.
8. T. Honeyands and J. Herbertson: *Steel Res.*, 1995, vol. 66 (7), pp. 287–93.
9. N.J. Lawson and M.R. Davidson: *J. Fluids Eng.*, 2002, vol. 124 (2), pp. 535–43.
10. D. Xu, W.K. Jones, and J.W. Evans: in *Processing of Metals and Advanced Materials: Modeling, Design and Properties*, B.Q. Li, ed., TMS, Warrendale, PA, 1998, pp. 3–14.
11. S. Sivaramakrishnan, B.G. Thomas, and S.P. Vanka: in *Materials Processing in the Computer Age*, V. Voller and H. Henein, eds., TMS, Warrendale, PA, 2000, pp. 189–98.
12. H. Bai and B.G. Thomas: *Metall. Mater. Trans. B*, 2001, vol. 32B, pp. 253–67.

13. H. Bai and B.G. Thomas: *Metall. Mater. Trans. B*, 2001, vol. 32B, pp. 269–84.
14. D.E. Hershey, B.G. Thomas, and F.M. Najjar: *Int. J. Numer. Methods Fluids*, 1993, vol. 17 (1), pp. 23–47.
15. F.M. Najjar, B.G. Thomas, and D.E. Hershey: *Metall. Mater. Trans. B*, 1995, vol. 26B, pp. 749–65.
16. B.G. Thomas, L.J. Mika, and F.M. Najjar: *Metall. Trans. B*, 1990, vol. 21B, pp. 387–400.
17. X. Huang and B.G. Thomas: *Can. Metall. Q.*, 1998, vol. 37 (3–4), pp. 197–212.
18. K. Takatani, Y. Tanizawa, H. Mizukami, and K. Nishimura: *ISIJ Int.*, 2001, vol. 41 (10), pp. 1252–61.
19. Q. Yuan, B.G. Thomas, and S.P. Vanka: *Metall. Mater. Trans. B*, 2004, vol. 35B, pp. 685–702.
20. Q. Yuan, S. Sivaramakrishnan, S.P. Vanka, and B.G. Thomas: *Metall. Mater. Trans. B*, 2004, vol. 35B (5), pp. 967–82.
21. B.G. Thomas, Q. Yuan, S. Sivaramakrishnan, T. Shi, S.P. Vanka, and M.B. Assar: *ISIJ Int.*, 2001, vol. 41 (10), pp. 1262–71.
22. H. Versteeg and W. Malalasekra: *An Introduction to Computational Fluid Dynamics: The Finite Volume Method Approach*, Longman Scientific Technical, Essex, United Kingdom, 1995.
23. B.E. Launder and D.B. Spalding: *Mathematical Models of Turbulence*, Academic Press, London, 1972.
24. B.G. Thomas: in *Making, Shaping and Treating of Steel*, A.W. Cramb, ed., AISE Steel Foundation, Pittsburgh, PA, 2003.
25. Y.A. Meng and B.G. Thomas: *Metall. Trans. B*, 2003, vol. 34B, pp. 685–705.
26. B.T. Rietow: Master's Thesis, University of Illinois at Urbana–Champaign, Urbana, IL, 2007.
27. D. Creech: Master's Thesis, University of Illinois at Urbana–Champaign, Urbana, IL, 1999.
28. *FLUENT6.3-Manual*, ANSYS Inc., Lebanon, NH, 2007.
29. G.A. Panaras, A. Theodorakakos, and G. Bergeles: *Metall. Mater. Trans. B*, 1998, vol. 29B, pp. 1117–26.
30. B.E. Launder and D.B. Spalding: *Comput. Meth. Appl. Mech. Eng.*, 1974, vol. 3 (2), pp. 269–89.